Cell Reports, Volume *19*

Supplemental Information

Excitatory Microcircuits within Superficial Layers of the Medial Entorhinal Cortex

Jochen Winterer, Nikolaus Maier, Christian Wozny, Prateep Beed, Jörg Breustedt, Roberta Evangelista, Yangfan Peng, Tiziano D'Albis, Richard Kempter, and Dietmar Schmitz

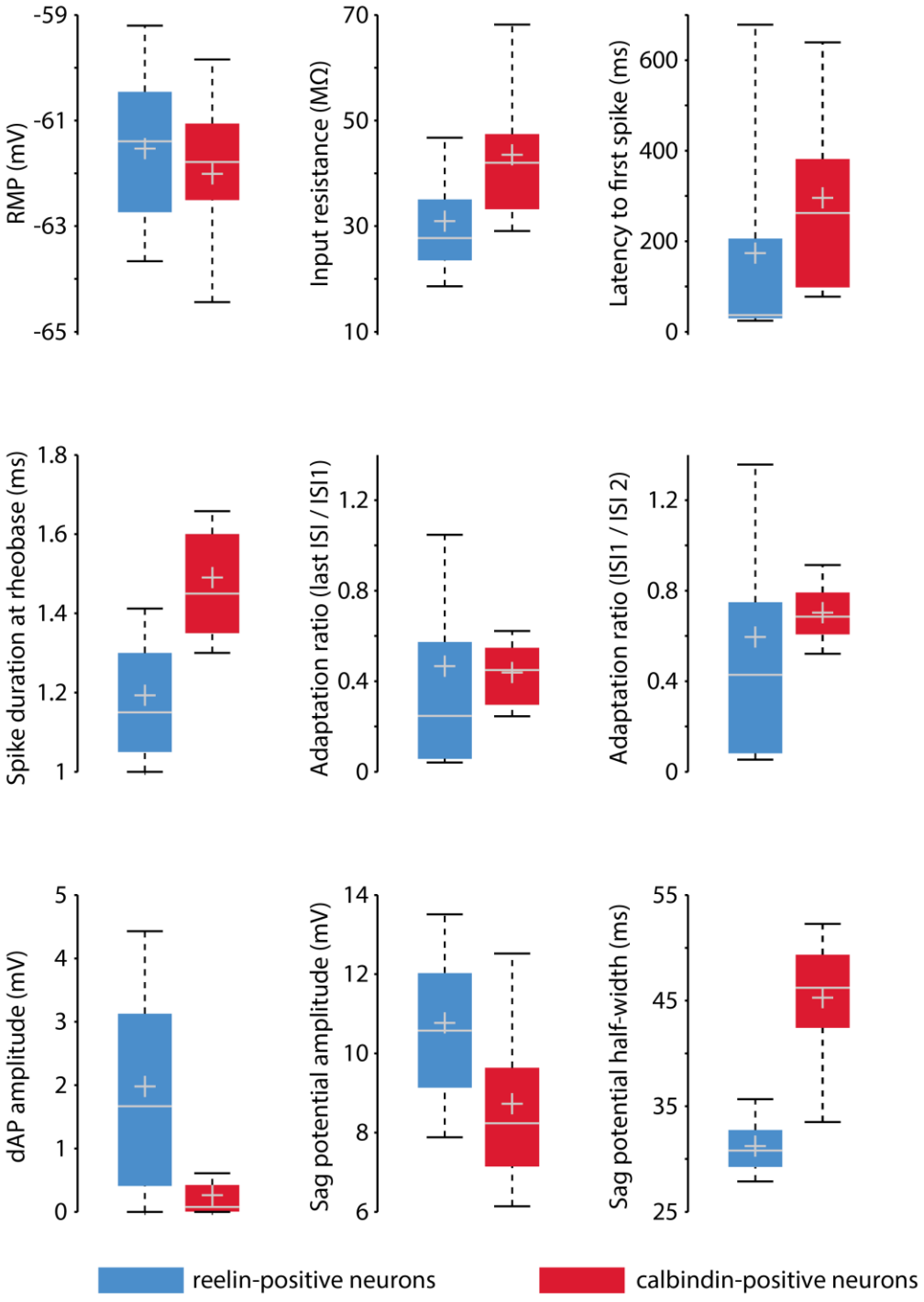

Figure S1. Intrinsic properties of reelin-positive and calbindin-positive cells in layer II of the entorhinal cortex, Related to Figure 1. Included are successfully stained cells, for which all nine intrinsic electrophysiological properties were recorded (n = 115 reelin-positive cells, blue, and n = 26 calbindin-positive cells, red). For details concerning the analysis of the respective parameter see **Supplemental Experimental Procedures** below. Box edges indicate the first and third quartiles, the median and the mean are given by the grey line and 'plus' symbols, respectively. Percentages spanned by the whiskers correspond to 9% and 91%, respectively.

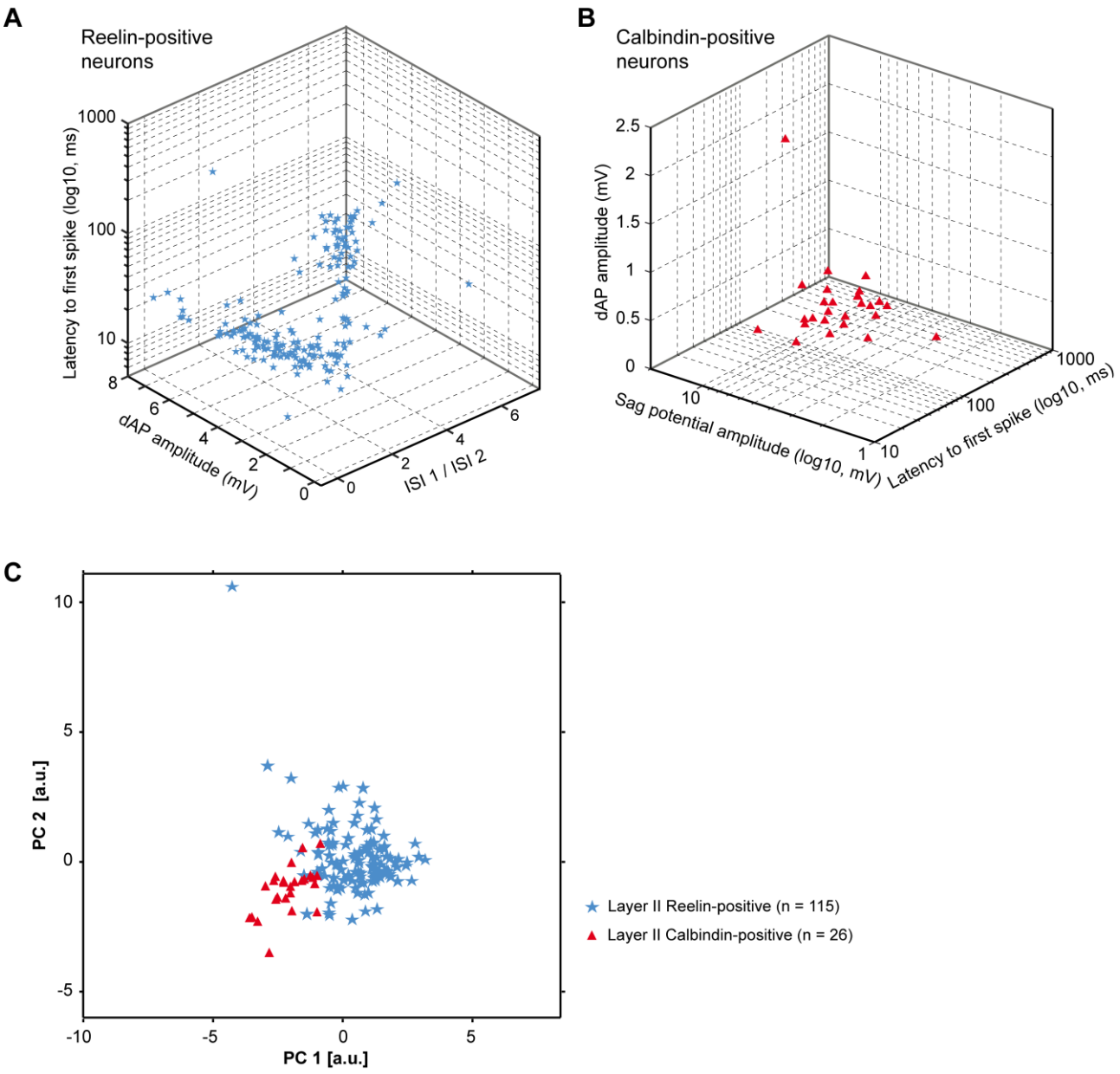

Figure S2. Absence of further categorization among reelin- and calbindin-expressing principal neurons in layer II of the MEC, Related to Figure 1. (A) For layer II stellate cells (n = 180) the distribution of three intrinsic parameters is plotted (as in Fuchs et al., 2016): the depolarizing afterpotential (dAP) amplitude, the latency to first spike, and the ratio of interspike interval 1 and interspike interval 2 (ISI 1 / ISI 2). Based on these criteria no further categorization of stellate cells was detected. **(B)** Similarly, the distribution of three intrinsic parameters in 27 identified (calbindin-expressing) layer II pyramidal neurons: depolarizing afterpotential (dAP) amplitude, latency to first spike, and sag potential amplitude, as in Fuchs et al., 2016. Based on these criteria, no further categorization of stellate cells was observed. **(C)** Principal component analysis performed on all nine intrinsic electrophysiological parameters. The projection on the first two principal components shows a clear separation between the two classes. Included are successfully stained cells for which all nine intrinsic electrophysiological properties were recorded (see also Figure S1 for display of all parameters).

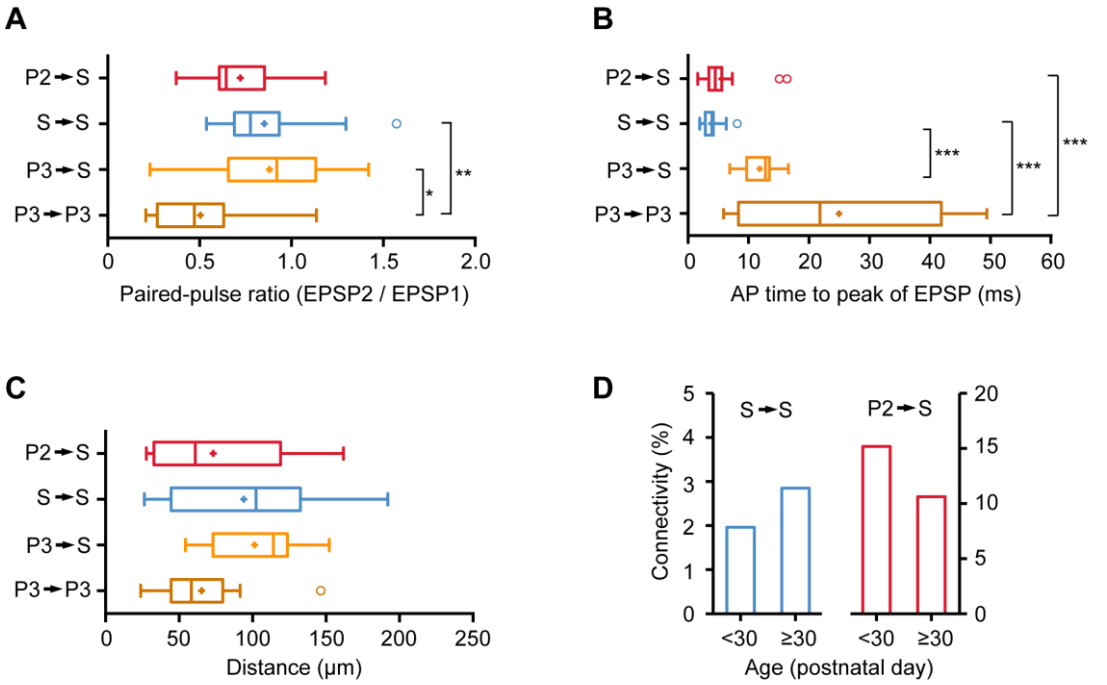

E

Connection / Connectivity / Study	lm PC ↓ PC	PC ↓ lm PC	lm PC ↓ SC	SC ↓ lm PC	lm PC ↓ lm PC	SC ↓ SC	lm SC ↓ SC	SC ↓ lm SC	PC ↓ SC	PC ↓ PC	SC ↓ PC	L2 ↓ L2	L3 ↓ L3
Dhillon & Jones 2000	n.t.	n.t.	n.t.	n.t.	n.t.	n.t.	n.t.	n.t.	n.t.	n.t.	n.t.	0% (0/135)	8.4% (33/393)
Couey et al. 2013	n.t.	n.t.	n.t.	n.t.	n.t.	0.2% (1/570)	n.t.	n.t.	0% (0/52)	n.t.	3.8% (2/52)	0.5% (3/674)	n.t.
Fuchs et al. 2015	7.5% (3/40)	4.8% (2/42)	10% (4/40)	0% (0/39)	4.7% (2/43)	0% 0/100	6.5% (3/46)	4.3% (2/47)	0% (0/38)	1.8% (1/56)	n.t.	3.5% (17/491)	n.t.
Present study	n.o.	n.o.	n.o.	n.o.	n.o.	2.5% (22/882)	n.o.	n.o.	10.6%* (24/226)	2.9%** (13/441)	0.4%*** (1/226)	3.3%**** (40 /1,198)	5.7% (12/209)

n.t. not tested n.o. not observed
* including L2PC→SC, L3PC→SC
** including L2PC→L2PC, L2PC→L3PC, L3PC→L2PC, L3PC→L3PC
*** including SC→L2 PC, SC→L3PC
**** including SC→SC, SC→L2PC, L2PC→SC, L2PC→L2PC

Figure S3. Properties of excitatory synaptic connections in the superficial layers of the MEC, Related to Figure 4. (A) Paired-pulse ratios (EPSP2/EPSP1) for the different groups. **(B)** AP time to peak for the different groups, measured as time from the peak of the presynaptic AP to the peak of the postsynaptic EPSP. **(C)** Distance of the connected cells, measured from the centers of the somata. **(D)** Connection probability between stellate cell – stellate cell (S→S) and layer II pyramidal cell – stellate cell (P2→S) at different ages. Age range from p21 to p29: (S→S) 2.0% (seven out of 356 connections tested) and (P2→S) 15.2% (12 out of 79 connections tested). Age range from p30 to p60: (S→S) 2.9% (15 out of 526 connections tested) and (P2→S) 10.6% (five out of 47 connections tested). Statistical significance of displayed differences was assessed by Dunn's test of multiple comparisons. * $P \leq 0.05$; ** $P \leq 0.01$; *** $P \leq 0.001$; **** $P \leq 0.0001$. Properties are shown only for contacts with more than one connection found. **(E)** Compilation of excitatory connectivity values in superficial layers of MEC based on previous studies. Numbers are gathered from Dhillon and Jones (2000), Couey et al. (2013) and Fuchs et al. (2015), and the present study. *Abbreviations:* SC: Stellate cell, Im SC: intermediate stellate cells, PC: pyramidal cells, Im PC: intermediate pyramidal cells, L2: layer II principal cells, L3: layer III pyramidal cells.

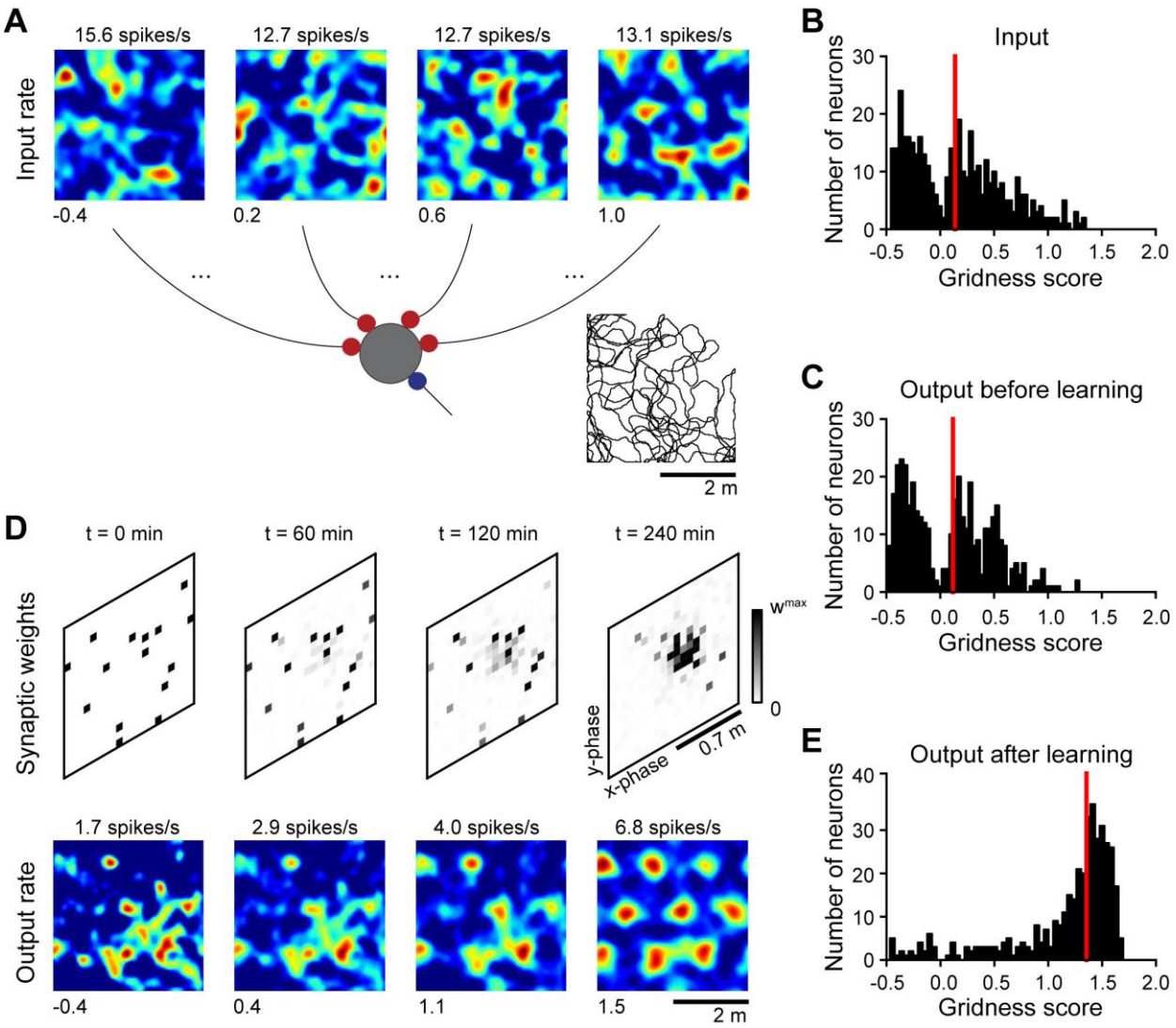

Figure S4. Improvement of grid tuning in a feed-forward network model, Related to Figure 4. **(A)** Model schematic. In a target principal-cell population, each output neuron (example: grey disc) receives feed-forward excitation (red discs) from N^{in} spatially tuned inputs and inhibition (blue disc) from spatially-untuned interneurons. At the top row, four examples of the input rate maps are shown (dark blue: 0 spikes/s, dark red: peak rate reported at the top, gridness score reported at the bottom left corner). Input rate maps are noisy hexagonal grids with common spacing and orientation but different phases. An example of the trajectory covered by a virtual-rat is shown at the bottom right (10 minutes of exploration). **(B)** Gridness scores of the excitatory inputs (N^{in} = 400, see examples in A). **(C)** Gridness scores of the outputs before learning, i.e., with random feed-forward weights (N^{out} = 400). **(D)** Development of the excitatory synaptic weights (top row, weights from 0 to w^{max} in grey scale) and corresponding output firing rate maps (bottom row) for one example output neuron. Four snapshots are shown (see simulation times at the top). Nearby pixels in the synaptic weight maps correspond to inputs with similar grid phases. Output rates are color-coded as in A. **(E)** Gridness scores of the outputs at the end of the simulation (t = 240 min). The red vertical lines in B, C, and E denote median gridness score values.

Supplemental Experimental Procedures

Cell classification. To differentiate layer II principal neurons, we made use of the differential immunoreactivity of these cells, i.e. stellate cells expressing the glycoprotein reelin and pyramidal neurons expressing the Ca^{2+} binding protein calbindin (Varga et al., 2010). Immunolabeling revealed 238 reelin-positive and 48 calbindin-positive cells, enabling us to classify them as stellate- and pyramidal neurons, respectively. We further analyzed nine electrophysiological parameters in all cells, if possible (Figure S1; see also Alonso and Klink, 1993; Canto and Witter, 2012): *Resting membrane potential* values represent initial voltages recorded after arriving in the whole-cell configuration. The *input resistance* was calculated from the deviation from baseline of steady-state voltage responses evoked by intracellular current injections (50 pA). The *latency to first spike* at rheobase was determined as the time from the onset of the depolarization step current to the onset of the action potential (threshold: $dV/dt \geq 90$ V/s). The *spike duration at rheobase* was found as the duration from spike onset to the time point where the decaying slope of the action potential crossed the onset voltage level again. The *adaptation ratio* was calculated both as the ratio of the last and the first interspike intervals (last ISI / ISI 1) or as the ratio of the first two interspike intervals (ISI 1 / ISI 2) at current steps of +500 pA and 1000 ms. The *depolarizing afterpotential (dAP)* for spikes at rheobase was determined by calculating the voltage difference between the local minimum of the fast afterhyperpolarization (fAHP) and the following depolarizing peak (Alonso and Klink, 1993). *Amplitude and half-width* (i.e., the duration at 50% of the amplitude) of the *sag potential* were measured in response to -750 pA (or -100 pA) current injection. We observed that the half-width of the sag potential -750 pA current injection predicted best the immunoreactivity to reelin and calbindin of layer II principal cells (Fig. S1). This enabled us to define a threshold for the classification of cells with non-sufficient staining. To find the best separation value, we used a linear 1d support vector machine (SVM, from the Python scikit-learn package, version 0.18.1) taking into account the class imbalance of reelin-positive and calbindin-positive cell numbers. The weighted SVM for the half-width of the sag potential was 37.2 ms (accuracy: 0.93; 10-fold cross validation) at -750 pA current injection (in some of the recorded cells we injected only -100 pA, yielding a weighted SVM of 45.2 ms with a slightly reduced accuracy: 0.85; 10-fold cross validation). Finally, we classified neurons that were non-sufficiently stained as follows: cells were classified as reelin-positive and therefore as stellate cells, if the half-width of the sag potential was ≤36 ms for -750 pA current injection (or ≤42 ms for -100 pA current injection) and as calbindin-positive and therefore as pyramidal cells if the half-width of the sag potential was ≥38 ms (-750 pA) or ≥48 ms (-100 pA). Layer III pyramidal cells could be easily distinguished from both layer II pyramidal and stellate cells based on clear differences in input resistance (mean ± SD: 124 ± 32 MΩ) and resting membrane potential (mean ± SD: -67 ± 5

mV) in layer III pyramidal cells (see Fig. S1 for comparison with layer II stellate and pyramidal neurons).

Modeling. Here we show that feed-forward excitatory projections could support the inheritance of grid-cell activity across distinct neuronal populations, and that grid patterns could become more regular through this inheritance process. To this end, we model the activity of a population of weakly-tuned grid cells projecting to a target principal-cell population as a virtual rat explores a square enclosure. Input firing-rate maps were obtained by distorting with noise hexagonal grids with common spacing and orientation, but different spatial phases (Fig. S4A, B), similarly to what is observed within a grid-cell module (Hafting et al., 2005). The feed-forward connectivity was sparse and initially random, that is, each neuron in the target principal-cell population received input from a set of noisy grids with random spatial phases. Such a random connectivity slightly decreased the grid tuning of the output spatial maps (Fig. S4C). Indeed, in a feed-forward network, the output grid tuning could be improved only by selecting input grids with similar phases. But how to obtain such an input selection that crucially depends on the behavioral correlates of neural activity?

We suggest that Hebbian plasticity could drive this selection. In Fig. S4D we illustrate this hypothesis for one example output neuron in the target principal-cell population. Initially, the output neuron was driven by a random set of inputs, and the corresponding output firing-rate map was spatially irregular (Fig. S4D, left-most panels). With experience, however, inputs with similar grid phases increased their synaptic strength, and, as a result, a more regular grid pattern emerged at the output (Fig. S4D, right-most panels). The spatial phase of the output grid depended on the initial state of the synaptic weights and on the trajectory of the virtual rat, which were both random. Nevertheless, regardless of the initial conditions, the firing-rate maps at the output (Fig. S4E) were consistently more regular than the ones at the input (Fig. S4B).

In summary, we demonstrate with a computational model that grid tuning could be inherited and even be improved via feed-forward projections across distinct principal-cell populations. We assumed that the experimentally observed feed-forward connections (Figs. 1-3) were also representative for grid cells and that cells with weak grid tuning (same period, same orientation, but different phase) in an input layer projected to a target grid cell in an output layer. Note that inheritance requires only weak grid tuning at the input layer (see input gridness scores in Fig. S4B).

A connectivity pattern suitable for the inheritance was learned from the activity correlations already present at the input. We suggest that such learning could happen concurrently with the development of grid cells in the first ~3 weeks of age (Langston et al., 2010; Wills et al., 2012, 2010), and that grid-field inheritance could take place in feed-forward projections from pyramidal cells in layer II or III to stellate cells in layer II. This is in line with recent reports that both stellate and pyramidal cells

show grid spatial tuning (Sun et al., 2015), although it remains unclear which principal-cell population contains the most-regular grids (Sun et al., 2015; Tang et al., 2014).

Model implementation.

We model a feed-forward network of N^{in} excitatory inputs with rates $\{ r_j^{\text{in}} : j = 1, 2, ..., N^{\text{in}} \}$ projecting to N^{out} excitatory outputs with rates $\{ r_i^{\text{out}} : i = 1, 2, ..., N^{\text{out}} \}$, where

$$r_i^{\text{out}}(\vec{x}) = \left[\sum_{j=1}^{N^{\text{in}}} w_{ij}\, r_j^{\text{in}}(\vec{x}) - r_0 \right]_+ . \tag{1}$$

The vector $\vec{x} = [x_1, x_2]$ is the position of the virtual rat in the environment, w_{ij} is the synaptic weight from input neuron j to output neuron i, $r_0 > 0$ spikes/s is a spatially-homogeneous inhibitory rate, and the function $[z]_+ = z$ if $z > 0$, $= 0$ if $z \leq 0$ is a static non-linearity. The input rates are modeled by distorting with noise hexagonal grids with common spacing and orientation, but different spatial phases:

$$r_j^{\text{in}}(\vec{x}) = \left[a g_j(\vec{x}) + (1 - a)\xi_j(\vec{x}) \right]_+ , \tag{2}$$

where $g_j(\vec{x})$ is a hexagonal grid with phase $\vec{\varphi}_j$, $\xi_j(\vec{x})$ is a realization of a 2-dimensional noise process, and the parameter $0 < a < 1$ weights the strength of the grid signal in relation to the noise. The grid signal $g_j(\vec{x})$ is the sum of three planar waves with wave vectors $\{\vec{k}_n : n = 0, 1, 2\}$ that are 60 degrees apart:

$$g_j(\vec{x}) = B \left[\sum_{n=0}^{n=2} \cos\left(\vec{k}_n \cdot \left(\vec{x} + \vec{\varphi}_j \right) \right) \right]_+ \quad \text{with} \quad \vec{k}_n = \frac{4\pi}{T\sqrt{3}} \begin{bmatrix} \cos(\, n\pi/3 + \beta\,) \\ \sin(\, n\pi/3 + \beta\,) \end{bmatrix} , \tag{3}$$

where $B > 0$ controls the grid amplitude, β sets the grid orientation, and T is the grid spacing. The spatial phases $\{\vec{\varphi}_j\}$ are sampled to cover the entire phase space evenly. The input noise is uncorrelated across neurons but correlated across spatial locations such that it varies smoothly in space. Specifically, the noise is generated by low-pass filtering 2-dimensional white Gaussian noise with a circularly-symmetric Gaussian filter: $G(\vec{x}) = \exp(-|\vec{x}|/2\,\sigma_x^2)$, where σ_x controls the filter width. The mean and the variance of the noise are normalized to match the ones of the input signal $g_j(\vec{x})$.

The excitatory synaptic weights $\{w_{ij}\}$ are changed according to the following Hebbian learning rule:

$$\frac{\mathrm{d}w_{ij}}{\mathrm{d}t} = \eta\left(r_j^{\mathrm{in}} - \gamma\right) r_i^{\mathrm{out}}, \tag{4}$$

where η is a small learning rate and $\gamma > 0$ spikes/s sets the threshold between long-term potentiation and long-term depression. Additionally, the synaptic weights $\{w_{ij}\}$ are bounded between 0 and $w^{\max}$ at each time point. At the initial condition, a random subset of $N^{\mathrm{up}} < N^{\mathrm{in}}$ synaptic weights are set at the upper bound $w^{\max} > 0$ whereas all the other weights are set to 0.

The virtual rat explores a square arena of side-length L with a correlated random walk with movement directions that vary smoothly in time. Precisely, the rat's trajectory is a sample of the 2-dimensional stochastic process

$$\frac{\mathrm{d}\vec{X}_t}{\mathrm{d}t} = v\,[\,\cos(\theta_t), \sin(\theta_t)\,] \quad \text{with} \quad \theta_t = \sigma_\theta W_t\,, \tag{5}$$

where $\vec{X}_t$ is the position of the virtual rat at time t, the process θ_t sets the direction of motion, and W_t is a standard Wiener process. The parameters v and σ_θ control the speed of motion and the tortuosity of the trajectory. At the boundaries of the environment, only movement directions towards the interior of the arena are retained.

Parameter values: $N^{\mathrm{in}} = N^{\mathrm{out}} = 400$, $r_0 = 3$ spikes/s, $a = 0.27$, $B = 6$, $\beta = 0$, $T = 1.4$ m, $\sigma_x = 0.15$ m, $\eta = 2 \cdot 10^{-5}$1/s, $\gamma = 3.8$ spikes/s, $w^{\max} = 0.067$, $N^{\mathrm{up}} = 15$, $L = 4$ m, $v = 0.2$ m/s, $\sigma_\theta = 0.7$.

Gridness scores of input and output firing-rate maps were computed with the algorithm proposed by (Stensola et al., 2012).

Supplemental References

Alonso, A., Klink, R. (1993). Differential electroresponsiveness of stellate and pyramidal-like cells of medial entorhinal cortex layer II. J. Neurophysiol. *70*, 128–143.

Canto, C.B., Witter, M.P. (2012). Cellular properties of principal neurons in the rat entorhinal cortex. II. The medial entorhinal cortex. Hippocampus *22*, 1277–1299.

Hafting, T., Fyhn, M., Molden, S., Moser, M., Moser, E.I. (2005). Microstructure of a spatial map in the entorhinal cortex. Nature *436*, 801–806.

Langston, R.F., Ainge, J.A., Couey, J.J., Canto, C.B., Bjerknes, T.L., Witter, M.P., Moser, E.I., Moser, M.-B. (2010). Development of the Spatial Representation System in the Rat. Science *328*, 1576–1581.

Stensola, H., Stensola, T., Solstad, T., Frøland, K., Moser, M.-B., Moser, E.I. (2012). The entorhinal grid map is discretized. Nature *492*, 72–8.

Sun, C., Kitamura, T., Yamamoto, J., Martin, J., Pignatelli, M., Kitch, L.J., Schnitzer, M.J., Tonegawa, S. (2015). Distinct speed dependence of entorhinal island and ocean cells, including respective grid cells. Proc. Natl. Acad. Sci. *112*, 9466–9471.

Tang, Q., Burgalossi, A., Ebbesen, C.L., Ray, S., Naumann, R., Schmidt, H., Spicher, D., Brecht, M. (2014). Pyramidal and stellate cell specificity of grid and border representations in layer 2 of medial entorhinal cortex. Neuron *84*, 1191–1197.

Varga, C., Lee, S.Y., Soltesz, I. (2010). Target-selective GABAergic control of entorhinal cortex output. Nat. Neurosci. *13*, 822–4.

Wills, T.J., Barry, C., Cacucci, F. (2012). The abrupt development of adult-like grid cell firing in the medial entorhinal cortex. Front. Neural Circuits *6*, 21. doi: 10.3389.

Wills, T.J., Cacucci, F., Burgess, N., O'Keefe, J. (2010). Development of the hippocampal cognitive map in preweanling rats. Science *328*, 1573–1576.